npj | quantum materials

Article

Published in partnership with Nanjing University

https://doi.org/10.1038/s41535-025-00806-y

Ramification of complex magnetism in $Nd_2Ir_2O_7$ observed by Raman scattering spectroscopy

Yuanyuan Xu[1], Yang Yang[2], Jérémie Teyssier[3], Takumi Ohtsuki[4], Yang Qiu[4], Satoru Nakatsuji[1,4,5,6,7], Dirk van der Marel[3], Natalia B. Perkins[2] & Natalia Drichko[1] ✉

Using Raman scattering spectroscopy, we uncover a complex magnetic behavior of $Nd_2Ir_2O_7$, which stands out among magnetic pyrochlores by the lowest temperature of the all-in-all-out (AIAO) Ir moments ordering ($T^N_{Ir} = 33$ K) and the highest temperature at which AIAO order of rare-earth Nd ions is detected (T^*_{Nd}=15 K). Detected magnetic Raman scattering and calculations of expected response allow us to demonstrate that the ordering of Ir magnetic moments is accompanied by an appearance of one-magnon Raman modes at 26.3 and 29.6 meV compatible with the AIAO order and allowing to estimate the energies of Ir-Ir interactions. An additional two-magnon excitation of the AIAO Nd order at around 33 meV appears in the spectra below the ordering temperature of Nd moments T^*_{Nd}=15 K. In the temperature range between 15 K and 33 K we observe a broad mode, which demonstrates strong temperature dependence and shifts on cooling below 20 K from 14 meV to higher frequencies, and disappears at 5 K, when two-magnon excitation of Nd moments becomes prominent. We suggest an interpretation of this excitation in terms of continuum arising from collective fluctuations of Nd moments above the transition. This complex behavior emerges from the interplay of strong spin-orbit coupling, electronic correlations, and geometric frustration on two magnetic pyrochlore sublattices of Nd and Ir ions.

Topological magnets provide a fertile platform to study novel phenomena through their nontrivial topological magnetic excitations[1–6]. Among them, magnetic Weyl semimetals with time reversal symmetry (TRS) breaking attract much attention due to their striking properties and a potential for various applications[7–12]. Pyrochlore iridates of general formula $R_2Ir_2O_7$ with R being a rare earth element Y, Eu, Nd, Sm, or Pr[3,13–17] were among the first materials predicted to host Weyl fermions[18]. In these materials, a Weyl semimetal state can be brought about by a splitting of the quadratic band touching node into pairs of Weyl nodes either under TRS breaking produced by magnetic ordering of Ir magnetic moments[18,19] or by a loss of inversion symmetry center[20]. Particularly, AIAO ordering of Ir^{4+} magnetic moments below $T^{Ir}_N = 33$ K preserves cubic symmetry but breaks TRS[21], please note a spread in the T^{Ir}_N values cited in literature[22,23] due to the extreme sensitivity of $Nd_2Ir_2O_7$ properties to Ir/Nd stoichiometry. There is a set of circumstantial evidence, demonstrating both quadratic band touching in $Nd_2Ir_2O_7$ at the Γ-point in the paramagnetic high-temperature regime[27] and signatures of a magnetic Weyl semimetal associated with TRS breaking due to magnetic ordering of Ir moments below T^{Ir}_N[23,28,29]. Recently we demonstrated that electronic Raman scattering reveals the quadratic bands above $T^N_{Ir} = 33$ K and the linear dispersion of Weyl nodes below T^N_{Ir}[30].

In $Nd_2Ir_2O_7$ not only Ir^{4+} but also Nd^{3+} ions are magnetic with $J = 9/2$. Their moments gradually order into AIAO state, which was experimentally observed below the crossover temperature T^*_{Nd}=15 K, as reported in previous studies[24,25,31]. This temperature stands out as an order of magnitude higher than the ordering temperatures for other Nd-containing pyrochlores[32–35], suggesting a strong coupling between Nd^{3+} and Ir^{4+} magnetic moments. Specifically, it was suggested that the AIAO order of Ir moments provides local magnetic field[36,37], gradually inducing the alignment of Nd moments into the AIAO order as the temperature decreases. Similar observations have been also reported in several pyrochlore iridates,

[1]Institute for Quantum Matter and Department of Physics and Astronomy, Johns Hopkins University, Baltimore, MD, USA. [2]School of Physics and Astronomy, University of Minnesota, Minneapolis, MN, USA. [3]Department of Quantum Matter Physics, University of Geneva, Geneva, Switzerland. [4]Institute for Solid State Physics, University of Tokyo, Kashiwa, Chiba, Japan. [5]Department of Physics, University of Tokyo, Bunkyo-ku, Tokyo, Japan. [6]Trans-scale Quantum Science Institute, University of Tokyo, Bunkyo-ku, Tokyo, Japan. [7]CREST, Japan Science and Technology Agency, Kawaguchi, Saitama, Japan.
✉e-mail: drichko@jhu.edu

such as $Ho_2Ir_2O_7$, $Tb_2Ir_2O_7$ and $Dy_2Ir_2O_7$[38–41], where both the ordering of Ir moments and the subsequent ordering of rare-earth moments have been observed at relatively high temperatures.

In this work, we present Raman scattering data and model calculations, which together identify a set of magnetic excitations in $Nd_2Ir_2O_7$ originated from strongly interacting Ir and Nd magnetic subsystems. We identify the one-magnon excitations from the AIAO ordering of Ir moments appearing below $T_{Ir}^{N} = 33$ K, and a band of two-magnon excitations of the AIAO order of Nd moments below the crossover temperature T_{Nd}^{*}=15 K. In the temperature range just below $T_{Ir}^{N} = 33$ K we observe a broad Raman excitation at about 14 meV, which shows unconventional temperature behavior, that allows us to associate it with the collective fluctuations of Nd moments. As a possible interpretation of this collective excitation observed at relatively high energies, we discuss a scenario where this high energy scale points to a notable renormalization of the magnetic interactions between Nd^{3+} ions. This renormalization could stem from either additional super-exchange pathways involving partially filled Ir^{4+} ions or from low-energy electronic excitations of the low-temperature Weyl semimetallic state[30,36], or both, and tends to the emergence of spin-ice[42–46] behavior in the Nd subsystem at intermediate temperatures. The complex interplay between renormalized exchange couplings of Nd moments, the local field exerted on Nd moments from the ordered AIAO state of Ir moments, and various factors such as strong spin-orbit coupling (SOC), electronic and magnetic correlations, and band topology collectively determines the unique low-temperature magnetic properties of $Nd_2Ir_2O_7$.

Results

Raman scattering spectra of $Nd_2Ir_2O_7$ in the temperature range from 50 K down to 7 K and spectral range between 3 and 40 meV were measured in (x, x) ($A_{1g} + E_g + T_{2g}$ scattering channels) and (x, y) ($E_g + T_{2g}$ channels) polarizations in the [111] crystal plane (see Fig. 1(b, c)). The spectroscopic response of $Nd_2Ir_2O_7$ and its temperature evolution are very rich, reflecting the complexity of the material. The spectra of $Nd_2Ir_2O_7$ in the paramagnetic semimetallic phase above 33 K show narrow intense features of phonons above 35 meV superimposed on a broad electronic scattering continuum. The observed phonon spectrum is in agreement with previously observed results from $Nd_2Ir_2O_7$ and other pyrochlore iridates[47–50]. Detailed discussions and assignments of the phonons can be found in the SI. The crystal electric field (CEF) excitations reported in previous studies of $Nd_2Ir_2O_7$[32,50–52] are also expected to manifest in the low-temperature Raman spectrum. Indeed, at 35 K we observed a very weak excitation at 25 meV (see Fig. 1b, c and Fig. 3g), see Section S1.3 of SI for more information. However, the overlap of this CEF excitation with the one magnon excitations M2 and M3, appearing in the spectra below 33 K, poses a challenge in studying its temperature evolution.

A phase transition at $T_{Ir}^{N} = 33$ K is manifested by an appearance of a number of new excitations in the spectra. Excitations at 26.3 and 29.6 meV (M2 and M3) appear in both polarization channels at temperatures slightly above T_{Ir}^{N}, increase in intensity below the transition, and show small changes in the position and width on cooling. This temperature evolution of M2 and M3 is consistent with the expected behavior of spin wave modes above a well-defined long-range magnetic order. Note that two one-magnon excitations at similar frequencies, 28.6 meV and 34.4 meV, were also observed $Y_2Ir_2O_7$[49].

A pronounced broad mode (M1) emerges below 33 K at 14 meV. This mode is only seen in the (x, x) channel, as depicted in Fig. 1b. This mode gains intensity on cooling the sample down to approximately 20 K. As the temperature continues to decrease, the mode undergoes a continuous shift towards higher energies, and its width increases, as illustrated in Fig. 1d. However, as the temperature falls below $T_{Nd}^{*} = 15$ K, this robust feature

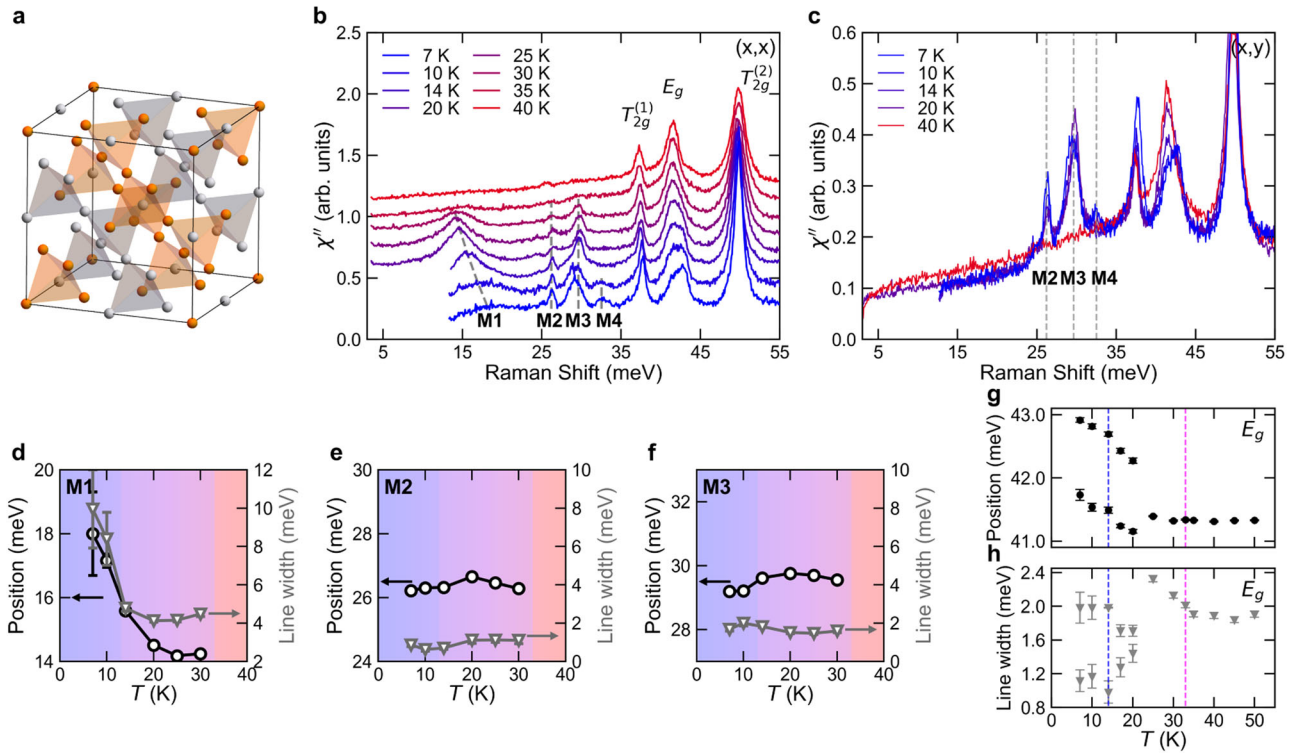

Fig. 1 | Temperature dependence of Raman scattering spectra of $Nd_2Ir_2O_7$. **a** Schematic structure of the pyrochlore $Nd_2Ir_2O_7$, with Nd ions shown in orange and Ir ions shown in grey. **b**, **c** Temperature dependence of Raman scattering spectra of $Nd_2Ir_2O_7$ in the spectra range between 3 and 55 meV, at temperatures between 40 K and 7 K. Spectral range below 20 K is limited by 12 meV: **b** (x, x) polarization, $A_{1g} + E_g + T_{2g}$ scattering channels. Note a shift of $\chi''(\omega)$ along Y axis for clarity; **c** (x, y) polarization $E_g + T_{2g}$ scattering channels. Magnetic excitations discussed in the text are labeled M1-M4; **d**–**f**. Temperature dependence of the position and line width of magnetic excitations M1, M2, and M3 peaks measured in the (x, x) polarization. The background colors, pink, magenta, and blue, mark, correspondingly, the temperature regions of the paramagnetic phase, Ir AIAO ordered phase, Ir and Nd AIAO ordered phase.**g**, **h** Temperature dependence of positions and line width of the E_g phonon and its two components observed at lower temperatures.

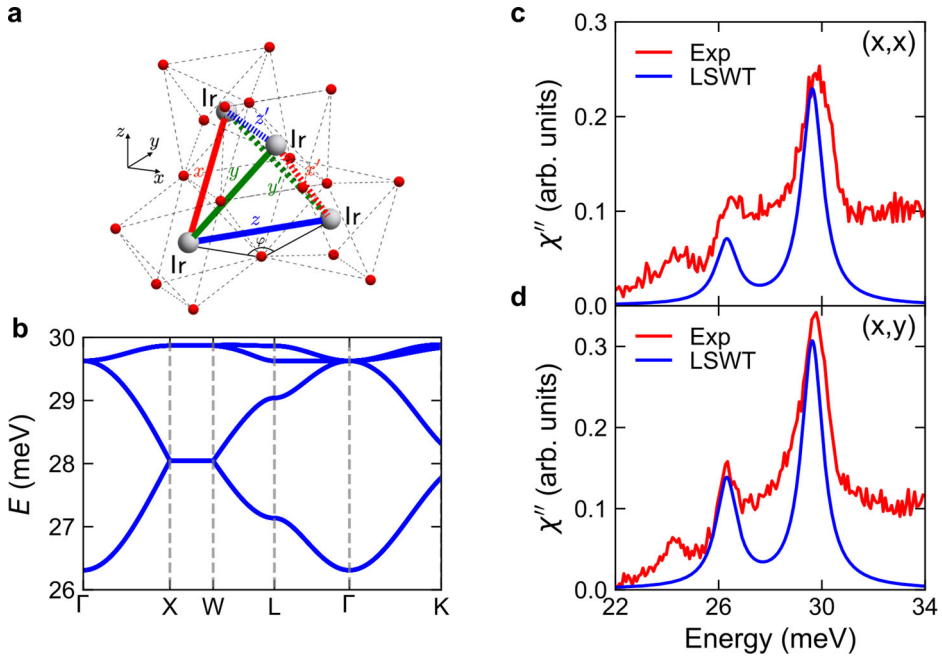

Fig. 2 | Raman scattering probed one-magnon excitations of AIAO ordered Ir sublattice in $Nd_2Ir_2O_7$. **a** A tetrahedron formed by Ir^{4+} ions: six different types of bonds are denoted by x, y, z, x', y', and z'. The surrounding oxygen ions of two neighboring Ir^{4+} ions form two tilted corner-sharing octahedra. The angle of Ir-O-Ir is denoted by φ. **b** Magnon band structure for the AIAO order of Ir moments obtained by the linear spin wave calculations. **c**, **d** Comparison of the experimental data (T = 20 K, red line) with the computed one-magnon Raman response (blue line). **c** Calculation is done for the parallel channel with arbitrary incoming light polarization in the [111] plane with $\mathbf{e}_{\text{in}}^{\parallel} = \mathbf{e}_{\text{out}}^{\parallel} = (0.80, -0.26, -0.54)$ for the parallel channel. **d** Calculation is done for the cross polarized channel with $\mathbf{e}_{\text{in}}^{\perp} = \mathbf{e}_{\text{in}}^{\parallel}$, $\mathbf{e}_{\text{out}}^{\perp} = (-0.16, 0.77, -0.61)$.

gradually disappears: while at 7 K, the continuum, although of significantly diminished in intensity, remains discernible; but at 5 K, as can be seen from the non-polarized Raman spectra presented in Fig. 3g, it totally disappears. Lastly, below 15 K, a weak peak feature (M4) emerges in both scattering channels, with an energy of ~33 meV.

The absence of the feature at 14 meV (M1) in the (x, y) scattering channel allows us to follow the change of the continuum of electronic scattering through the phase transition at T_{Ir}^{N} = 33 K. The interpretation of the frequency dependence of the electronic continuum in terms of the interband excitations between quadratic bands ($T > T_{\text{Ir}}^{\text{N}}$) and Weyl bands ($T < T_{\text{Ir}}^{\text{N}}$) is discussed elsewhere[30].

The temperature dependence of the phonons typically allows to uncover the lattice response to magnetic ordering and changes in the electronic structure. The largest changes are observed for E_g phonon at 42 meV (Fig. 1g, h). The changes onset at T_{Ir}^{N} = 33 K marked by the magenta dashed line in the figure, when the splitting of the E_g phonon is too small to resolve (Fig. 1g). Below 20 K, where the splitting of 2 meV between the components is larger than the line width, we can clearly resolve the doublet. The spectral weight is shifted to the higher frequency component on further cooling [Fig. 1(b, g)]

Discussion

To understand the Raman spectra of $Nd_2Ir_2O_7$ below 33 K, we start with analyzing the existing information on its magnetic response. The data on the low-temperature magnetic order of the Nd and Ir sublattices were obtained by the neutron diffraction[24,31] and muon-spin relaxation (μSR) experiments[2,5,26,53]. While there are discrepancies in the exact size of magnetic moment of Nd^{3+}, all these studies agree on the AIAO at 2 K. Moreover, there is a consensus that the order starts developing already below 15 K, suggesting the effect of a local magnetic field on the Nd^{3+} moments, probably caused by the magnetic ordering of Ir. The magnetic structure of the Ir^{4+} sublattice is hard to probe by neutrons; however the combined evidence from the resonant X-ray scattering and μSR spectroscopies of pyrochlore iridates, including $Nd_2Ir_2O_7$, suggests that Ir^{4+} moments are ordered in the AIAO, parallel to the surrounding net of Nd^{3+} moments[25,26,54,55].

Magnetic excitations of Ir^{4+} ions.–The M2 and M3 modes appear at T_{Ir}^{N} and are likely to originate from the one-magnon excitations of AIAO ordered Ir^{4+} magnetic moments. To obtain the magnon spectrum, we first derive the superexchange interactions between effective spin-1/2 pseudospins of Ir^{4+} ions assuming the perfect octahedral oxygen environment on the pyrochlore lattice and following the steps outlined in refs. 56,57. The resulting superexchange Hamiltonian takes the following form:

$$\mathcal{H}_{\text{Ir-Ir}} = \sum_{\langle ij\rangle_\nu} \Big[J\,\mathbf{S}_i \cdot \mathbf{S}_j + K\,S_i^{\alpha_\nu} S_j^{\alpha_\nu} + \sigma_\nu \Gamma_{ij} \left(S_i^{\beta_\nu} S_j^{\gamma_\nu} + S_i^{\gamma_\nu} S_j^{\beta_\nu}\right) + \mathbf{D}_{ij} \cdot (\mathbf{S}_i \times \mathbf{S}_j) \Big], \tag{1}$$

where ν determines the type of the bond [Fig. 2a], and we have $(\alpha_\nu, \beta_\nu, \gamma_\nu)$ = (x, y, z), (y, z, x), (z, x, y) for $\nu \in (x, x')$, (y, y'), (z, z'), respectively. The prefactor σ_ν equals +1 for $\nu \in (x, y, z)$ and -1 for $\nu \in (x', y', z')$. The form of (1) is also in agreement with the superexchange Hamiltonian obtained from the symmetry consideration in Ref.[19]. Given the bond-dependent anisotropy of the Hamiltonian and the non-collinear nature of the AIAO order, the one-magnon response is expected to dominate the low-energy Raman spectrum[58]. The AIAO state on the pyrochlore lattice gives rise to two magnon modes at center of the Brillouin zone (BZ) $\mathbf{k}$ = 0: one is non-degenerate and the other is three-fold degenerate with the degeneracy protected by the symmetry of the AIAO state on the pyrochlore lattice[59]. The calculated linear spin wave spectra provide a good agreement with the experimental data with the following set of parameters: (J, K, Γ, D) = (6.1, −5.4, 3.0, 4.1) meV, producing Γ-point one magnon modes at 26.3 and 29.6 meV (are shown in Fig. 2b). We computed the one-magnon Raman response within the Loudon-Fleury approach[60], in which the Raman operator mirrors the processes governing exchange interactions but with virtual electron hopping being assisted by photons. It can be written as $\mathcal{R}_{\text{Ir}} = \sum_{\langle ij\rangle} (\mathbf{e}_{\text{in}} \cdot \mathbf{r}_{ij})(\mathbf{e}_{\text{out}} \cdot \mathbf{r}_{ij})\, \mathcal{H}_{\text{Ir},ij}$, where $\mathbf{e}_{\text{in}}(\mathbf{e}_{\text{out}})$ is incoming (outgoing) polarization of light, and $\mathbf{r}_{ij}$ denotes the vector connecting site i and j of Ir ions. Traditionally, it was believed that the Loudon-Fleury response results primarily in the two-magnon scattering with $\Delta S^z = 0$, involving the creation or destruction of a pair of magnons. However, this perspective is not universally applicable. It was recently shown[58] that in strongly correlated Mott insulators with spin-orbit coupling and bond-dependent anisotropic interactions, a one-magnon response naturally emerges. This is also true here.

Our results for the parallel and the cross polarized channels reproduce well the two bands M2 and M3 (Fig. 2c, d). As a consequence of the 3:1 ratio of degeneracies of the one-magnon

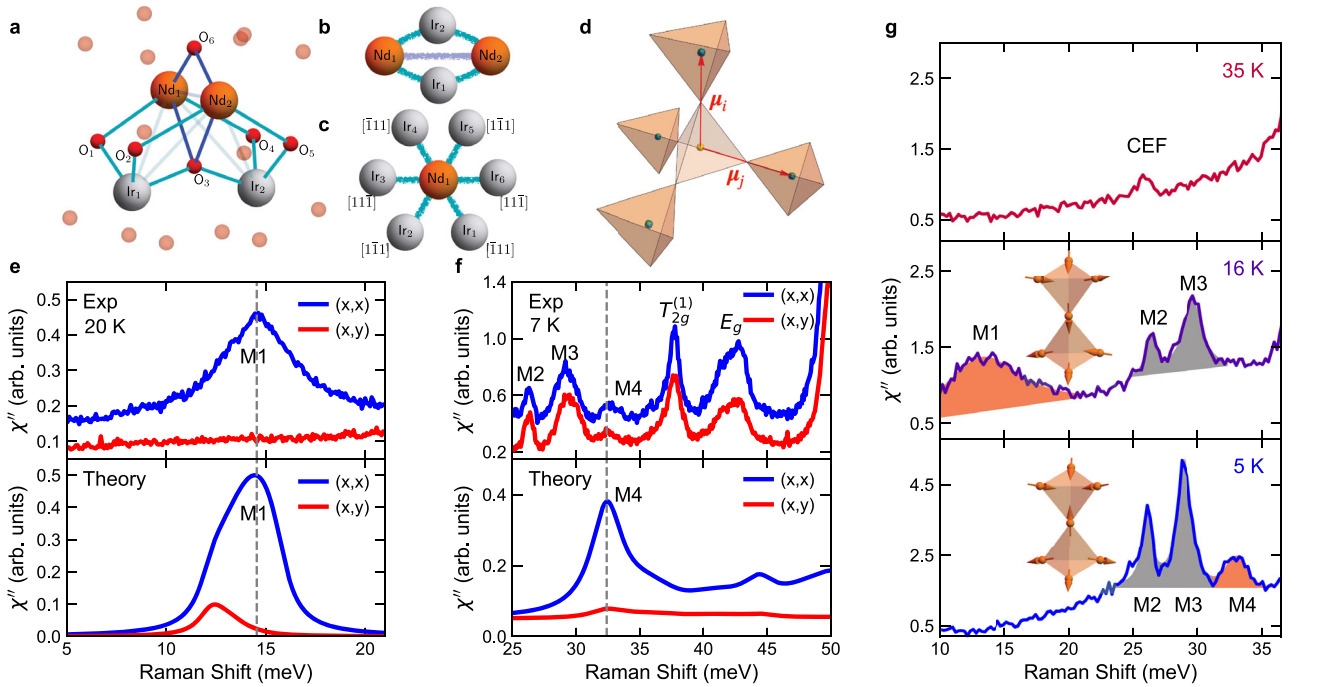

Fig. 3 | Raman scattering probed magnetic excitations of Nd sublattice in $Nd_2Ir_2O_7$. **a** Local environment of Nd-Nd superexchange interaction, blue bonds denote the original superexchange paths without Ir ions, and teal bonds indicate additional superexchange paths involve Ir ions. **b** Schematic representation of Nd-Nd superexchange interaction, the Nd-Nd superexchange (blue) is renormalized by the additional superexchange paths involving Ir ions (teal). **c** Schematic representation of a Nd ion surrounded by its six nearest neighboring Ir ions, where the directions of the AIAO-ordered Ir moments are given in the global reference frame. **d** Spinons are created on the diamond lattice (A and B sublattices of Nd tetrahedra are shown in light and dark orange, respectively) formed by the centers of Nd tetrahedra. **e** A comparison of the experimental data (upper panel) with the computed Raman response from the two-spinon continuum (lower panel). Two-spinon Raman response is computed for the parallel channel (blue curve) for an arbitrary incoming light polarization in the [111] plane $[\mathbf{e}_{\text{in}}^{\parallel} = \mathbf{e}_{\text{out}}^{\parallel} = (0.80, -0.26, -0.54)$ and for the cross channel (red curve) with $\mathbf{e}_{\text{in}}^{\perp} = (0.80, -0.26, -0.54)$, $\mathbf{e}_{\text{out}}^{\perp} = (-0.16, 0.77, -0.61)$. The results are in a good agreement with the experimental data ($T = 20$ K), where only the parallel channel gives a strong Raman intensity. **f** A comparison of the experimental data at $T = 7$ *K* (upper panel) with the computed Raman response from the two-magnon excitation of all-in-all-out ordered Nd moments (M4). Two-magnon Raman response computed for the same light polarizations as in (**e**). In the experimental data M4 feature is weak compared to other observed excitations. **g** A summary of experimental Raman spectra of $Nd_2Ir_2O_7$ in three different states: in paramagnetic semimetalic state at $T = 35$ *K*, crystal field excitation (CEF) of Nd is observed at 25 meV, at $T = 16$ *K*, where M1 feature of Nd-spinon continuum is observed together with one-magnon excitations of Ir M2,M3; And in the state where both Nd and Ir moments are ordered all-in-all-out at $T = 5$ *K*. Note that M2 and M3 one-magnon excitations of Ir are found at the same frequencies as at $T = 16$ *K*, while M4 two-magnon excitation of Nd order appears instead of the spinon continuum (insets depict the 2I2O state and AIAO state of Nd moments, respectively). All three plots are showing the Raman response in (x,x) channel.

excitations at the Γ-point, the computed intensity of the 29.6 meV one-magnon peak is higher than of the 26.3 meV peak, in agreement with the experiment. Moreover, the one-magnon peak M2 corresponds to the 1D irreducible corepresentation (for simplicity, we still refer them as "irrep") of $m\bar{3}m'$ magnetic point group, which is derived from the 2D irrep E_g of the paramagnetic group.

A continuum of two-magnon excitations expected within the Loudon-Fleury theory is absent in the Raman spectra of $Nd_2Ir_2O_7$ despite the flat magnon bands (Fig. 2b) which would result in a peak at around 65 meV. Two-magnon excitation was also not observed in $Eu_2Ir_2O_7$[48], and some other pyrochlore iridates[61]. This energy range overlaps with the interband electronic excitations[30], which can mask the observation of the two-magnon band.

Magnetic response of Nd^{3+} sublattice.– In contrast to iridium sublattice which was not probed by neutron scattering, neutron scattering was successfully used to probe crystal field excitations of Nd^{3+}, with first excited state at 25 meV, and second at 40 meV[51]. Also, a splitting of the ground state doublet of Nd^{3+} ions resulting in a 1.3 meV mode with weak dispersion in an AIAO state was detected[24,51]. In our Raman spectra in both (x,x) and (x,y) scattering channels the lowest crystal field excitation at around 25 meV is observed above T_{Ir}^{N} (see Fig. 3 g, ref. 62, and SI), and is barely distinguished at lower temperatures due to the more intense M2 magnon of Ir AIAO order at close frequencies. Phonons at around 40 meV obscure the second excitation in Raman scattering.

Additionally, with Raman scattering spectra measured to much higher energies than neutron scattering, we observe that M4 excitation appears at energies around 33 meV below T_{Nd}^{*} in both polarizations [see Figs. 1(b, c) and 3g].

A fully ordered AIAO state for Nd^{3+} moments is confirmed at 2 K by neutron scattering measurement. A comparison with the well-studied spin dynamics of $Nd_2Zr_2O_7$[63–65] and $Nd_2Hf_2O_7$[66] reveals that the Nd^{3+} moment's dynamics in $Nd_2Ir_2O_7$ occurs at significantly higher energy and temperature scales. This difference arises because the magnetic ordering of the Ir^{4+} ions on the B-sites provides both a local field and a renormalization of the exchange couplings of the Nd^{3+} moments, in contrast to the non-magnetic B-site ions in $Nd_2Zr_2O_7$ and $Nd_2Hf_2O_7$. In this sense, below 33 K, the ordered Ir^{4+} moments strongly influence the dynamics of the Nd^{3+} moments. Within a mean-field picture, this local field is proportional to the net effective magnetic moment, $\langle S_{\text{net,Ir}}^{z} \rangle$, generated by six neighboring Ir moments, $\langle m_{\text{Ir}} \rangle$, which point along the local z-axis (one of the global [111] directions) at each Nd site[37,67] [see Fig. 3c]. The net moment acting on Nd ion is equal to $\langle S_{\text{net,Ir}}^{z} \rangle = 2\langle m_{\text{Ir}} \rangle / \mu_B$ because four out of six neighboring Ir moments sum up to zero. At temperatures just below 33 K, the AIAO ordered moment in Nd subsystem is small due to the smallness of $\langle S_{\text{net,Ir}}^{z} \rangle$, but it becomes more pronounced at lower temperatures as $\langle S_{\text{net,Ir}}^{z} \rangle$ and, consequently, the net local field increase.

The AIAO order induced by the local field h_{loc} would, by itself, represent a purely local effect. In contrast, the additional mode M4 observed

in Raman scattering below T^*_{Nd} at 33 meV exhibits an energy and temperature dependence characteristic of a two-magnon Raman response associated with the AIAO-ordered Nd^{3+} moments. This mode is a collective excitation and indicates relatively strong interactions between Nd moments. To fully understand this behavior, it is necessary to formulate the complete renormalized Hamiltonian for the Nd^{3+} magnetic moments:

$$\begin{aligned}\mathcal{H}_{\mathrm{Nd}} &= \mathcal{H}_{\mathrm{Nd-Nd}} + \mathcal{H}_{\mathrm{Nd-Ir}} \\ &= \sum_{\langle ij \rangle} J_x \tau_i^x \tau_j^x + J_y \tau_i^y \tau_j^y + J_z \tau_i^z \tau_j^z - h_{\mathrm{loc}} \sum_i \tau_i^z, \end{aligned} \quad (2)$$

Here $\mathcal{H}_{\mathrm{Nd-Nd}}$ takes into account the renormalization of interactions between Nd^{3+} from Ir^{4+} ions. The local environment of Nd magnetic moments, schematically depicted in Fig. 3a, b, shows how partially filled extended 5d orbitals of Ir^{4+} ions provide many additional superexchange paths between Nd^{3+} ions, renormalizing exchange interactions.

The renormalization of magnetic interactions between rare-earth atoms through hybridization with the extended orbitals of non-rare-earth atoms is not unique to iridates. Interactions between Nd^{3+} magnetic moments renormalized by Cu^{2+}-Nd^{3+} interactions are suggested for magnetic behavior Nd_2CuO_4. In fact, a competition between Cu^{2+}-Nd^{3+} and Nd^{3+}-Nd^{3+} is suggested to be temperature dependent[68]. Another scenario of renormalized interactions between rare earth atoms through RKKY interactions with Weyl electrons is exemplified by Weyl semimetals NdAlSi[69,70] and CeAlSi[71]. In application to $Nd_2Ir_2O_7$, this concept is partially illustrated in the Supplemental Information in r ef.[36], which suggests that weak electron correlations on the Ir sites enhance the relative importance of Kondo-like interactions between the Ir and Nd subsystems. Interestingly, ref. 36 also proposes that such interactions favor 2I2O spin configurations for Nd moments over the AIAO order.

We use the Hamiltonian (2) to compute two-magnon response M4 of the AIAO Nd^{3+} order (Fig. 3f) The absence of $\tau^z\tau^x$ and $\tau^z\tau^y$ terms in the minimal model rules out the one-magnon excitation origin of M4. To compute two-magnon Raman responses of M4, we also incorporate a small anisotropy between J_x and J_y,. The observation of the two-magnon excitation at 33 meV below T^*_{Nd} suggests that interactions between Nd moments are strongly renormalized, reaching energy scales on the order of a few meV. We also note that the calculated intensity of the two-magnon response exhibits a stronger polarization dependence than that observed experimentally (see Fig. 3e, f). This discrepancy may be related to the use of the Loudon-Fleury approximation[60] in our calculations. In particular, the multiple superexchange paths giving rise to the effective superexchange couplings in Hamiltonian (2), illustrated in Fig. 3a, can give rise to non-Loudon-Fleury terms in the Raman operator, which may contribute substantially in the cross-polarization channel[58]. Such contributions could significantly modify the polarization dependence. However, considering these terms in this case is a challenging task that lies beyond the scope of this paper.

Magnon-spinon dichotomy of Nd^{3+} excitations.– Now we will discuss the M1 excitation at 14 meV present in the intermediate temperature regime between ordering temperatures of Ir and Nd magnetic moments. This excitation appears below T^N_{Ir} and remains relatively sharp only in a narrow temperature region (Fig. 1b, d). We can rule out a phonon origin for M1[50], as well as crystal field excitations of Nd^{3+}[62]. Furthermore, M1 cannot be attributed to magnetic excitations of the Ir ions, as those are well captured by the M2 and M3 modes discussed earlier in the manuscript, which show only minor changes below 33 K. The fact that M1 mode gradually disappears below the crossover temperature into the AIAO order of Nd^{3+} magnetic moments, combined with its broad, continuum-like spectral width, suggests that M1 originates from excitations of the disordered phase of the Nd^{3+} moments.

However, we also cannot associate the M1 feature in the Raman response spectrum with fluctuations of the AIAO order. While there are multiple examples of two-magnon responses persisting above the magnetic transition[72], including the two-magnon scattering observed across the AIAO transition in the insulating pyrochlore $Cd_2Os_2O_7$[73], the behavior of M1 in $Nd_2Ir_2O_7$ is distinctly different. The M1 excitation, appearing around 14 meV, cannot be the fluctuating remnant of the M4 two-magnon mode associated with Nd^{3+} AIAO order, because it emerges at a much lower energy than expected for fluctuating two-magnon scattering and is significantly more intense than M4. Moreover, if M1 originated from fluctuations of the AIAO order, it would be expected to preserve the same symmetry as M4 and appear in both polarizations. Instead, M1 is observed only in the (x,x) polarization channel. These observations strongly suggest that M1 must have a different origin.

Unfortunately, the origin of this magnetic continuum remains unresolved. We speculate that the continuum of excitations observed at 14 meV in the Raman response at intermediate temperatures could arise from fluctuations associated with the spin-ice-like phase of Nd^{3+} moments, analogous to the behavior observed in $Nd_2Zr_2O_7$, where 2I2O fluctuations persist above the AIAO ordering temperature[65,74].

In such a fluctuating 2I2O regime, the system supports collective excitations, including gapped, deconfined spinons and emergent gapless gauge modes, often referred to as emergent photons[42,45,46]. The Raman response from this phase is expected to be dominated by the spinon excitations revealing themselves in the form of a broad two-spinon continuum [46]. If a similar fluctuating 2I2O state develops in $Nd_2Ir_2O_7$ at intermediate temperatures, it could naturally account for the broad continuum-like Raman response observed at 14 meV, distinct from both phonon's features and conventional two-magnon excitations associated with AIAO ordering.

As a result, magnetism of Nd sublattice below T^N_{Ir} is governed by a competition between renormalized Nd-Nd interactions, which favor 2I2O order, and the local field h_{loc} generated by AIAO ordered Ir^{4+} moments. At temperatures near 33 K, $\langle S^z_{net,Ir}\rangle$ is small, and the system predominantly exhibits a 2I2O ice state with only a small fraction showing AIAO order. On cooling down, $T^*_{Nd} < T < T^N_{Ir}$, $\langle S^z_{net,Ir}\rangle$ increases, progressively driving more Nd moments into the AIAO state through the local field, leading to a strong temperature dependence of the M1 feature. Below 15 K, the prevalence of 2I2O correlations diminishes, and the Raman response becomes dominated by magnon excitations associated with the fully developed AIAO order of the Nd^{3+} moments. The competition between the 2I2O spin-ice phase and AIAO order is further explored in the Supplementary Information, where we analyze a minimal model that includes superexchange interactions favoring the 2I2O phase and a local field from the ordered Ir sublattice that supports AIAO order of Nd moments. We also derive the excitation spectrum of gapped spinons, which contribute to the Raman response.

The Raman response from the two-spinon excitation continuum in the parallel and cross polarizations shown in the lower panel Fig. 3e, with the incoming and outgoing light polarization same as in the case of the one-magnon response shown in Fig. 2c, d,is computed using the Raman operator for the QSI derived in ref. 46:

$$\mathcal{R}_{\mathrm{Nd}} = \sum_{\langle ij \rangle} \Big[(\mathbf{e}_{\mathrm{in}} \cdot \boldsymbol{\mu}_i)(\mathbf{e}_{\mathrm{out}} \cdot \boldsymbol{\mu}_i) + (\mathbf{e}_{\mathrm{in}} \cdot \boldsymbol{\mu}_j)(\mathbf{e}_{\mathrm{out}} \cdot \boldsymbol{\mu}_j) \Big] \mathcal{H}^{ij}_{\mathrm{Nd}}, \quad (3)$$

where $\boldsymbol{\mu}_i$ and $\boldsymbol{\mu}_j$ denote the relative position vectors of spinons associted with $\mathcal{H}^{ij}_{\mathrm{Nd}}$ (see Fig. 3d). In our calculation, we set the effective couplings of Nd magnetic moments j=1/2 to J_z = 12.0 meV, J_{xy} = − 3.0 meV, and the local field to h_{loc} = 12.0 meV. For these parameters, the resulting two-spinon Raman response qualitatively reproduces the main features of the M1 band shown in the upper panel of Fig. 3(e), with strong Raman intensity appearing only in the parallel polarization channel.

Splitting of 42 meV E_g phonon.– Lastly, we would like to address the distinctive aspects of the phonon dynamics observed in our Raman data. Below T^{Ir}_N, the changes in the phonon spectrum become evident, most notably in the E_g phonon at around 42 meV. On cooling, this phonon broadens and splits, with the spectral weight shifting towards the higher frequency component (see Fig. 1(b, g)). These observations provide insights into how the lattice of $Nd_2Ir_2O_7$ responds to the magnetic ordering and the changes in the electronic structure. While a separate study is required to fully

understand the lattice response in such a complex system as $Nd_2Ir_2O_7$ featuring two interacting magnetic sublattices and a complex electronic structure, here we provide some qualitative description.

The observed lattice response can stem from two main scenarios: (i) magneto-elastic coupling and (ii) electron-phonon coupling. In the first scenario, the magneto-elastic coupling arises from the dependence of the coupling between magnetic moments on the distance between them. It is usually large in the systems with strong spin-orbit coupling. In the paramagnetic phase, the E_g phonon couples to the linear combinations of magnetic bond energies transforming under the compatible 2D irrep of the paramagnetic group. Below the AIAO ordering transition, since phonons and magnetic fluctuations are linearly coupled by magneto-elastic coupling, the system's symmetry reduces to $m\bar{3}m'$, in which 2D irrep E_g splits into two distinct 1D irreps. Subsequently, one of the two phonons couples with the compatible one-magnon mode, M2, resulting in the splitting of the E_g phonon mode of the paramagnetic phase below T_{Ir}^N. It is essential to note that this phenomenon is solely dynamical and doesn't necessarily induce lattice distortion. Further details regarding the symmetry analysis can be found in Section S2 of the SI.

In the second scenario, the splitting of the E_g phonon modes is attributed to electron-phonon coupling. Although we do not believe this scenario applies to $Nd_2Ir_2O_7$, previous investigations in other iridium pyrochlores, like $Pr_2Ir_2O_2$[50] and $Eu_2Ir_2O_2$[48], have indicated that electron-phonon coupling can significantly impact phonon dynamics.

In conclusion, the complex temperature dependence of the Raman response in the magnetic pyrochlore $Nd_2Ir_2O_7$ reveals the intricate interplay between electronic, magnetic, and lattice degrees of freedom. Below $T_{\mathrm{N}}^{\mathrm{Ir}}$, we observe the appearance in the spectra of the Γ-point magnons of AIAO ordered Ir moments. Our calculations, fitted to the observed magnon frequencies, identify the key parameters of the magnetic interactions between Ir^{4+} moments.

The AIAO ordering of Nd^{3+} moments sets in at a relatively high temperature and is accompanied by an appearance of an additional excitation at 33 meV, which we assign to the two-magnon excitation of this order. This suggests that the coupling between the Ir and Nd sublattices significantly enhances the interactions between Nd^{3+} moments. We speculate that a broad Raman feature centered at 14 meV in the intermediate temperature range ($20\,\mathrm{K} < T < T_{\mathrm{Ir}}^N$) could represent a collective excitation from 2I2O fluctuations of Nd^{3+} moments driven by the enhanced interactions.

It is worth noting the similarity with a rare earth Weyl semimetal NdAlSi in the hierarchy of magnetic transitions, where antiferromagnetic incommensurate order is observed below 7.2 K, and a ferrimagnetic transition into commensurate state at 3.3 K[69]. Even for these systems with only one magnetic sublattice, final agreement upon the source of renormalized interactions is reached, with ab initio calculations suggesting an enhanced through orbital hybridization superexchange scenario[75].

This enhancement of Nd-Nd interactions makes $Nd_2Ir_2O_7$ an intriguing platform for exploring rare-earth magnetism and potentially quantum spin ice physics.

Methods

$Nd_2Ir_2O_7$ single crystals were grown by the KF-flux method[76] and possess as-grown octahedron-shaped (111) facets. Raman scattering spectra were collected from (111) cleaved surface of a single crystal of $Nd_2Ir_2O_7$ using two different Raman setups. The first setup allowed us to measure non-polarized Raman spectra in the temperature range from 300 to 5 K and in the spectral range down to 10 meV. Selected spectra from these measurements are shown in Fig. 3g. The measurements were done using Horiba Labram HR Evolution spectrometer equipped with Olympus microscope and an ultra narrow notch filter. The spectra were excited using a 532 nm laser radiation. Sample was placed in a He flux cryovac micro Konti cryostat. The exact temperature of the sample was obtain by a comparison of Stokes and anti-Stokes intensities.

Table 1 | Components of Raman tensor for (*x*, *x*) and (*x*, *y*) polarizations in measurements geometry when polarization *x* and *y* of electrical vectors e_{in} and e_{out} are parallel to the [111] crystalographic plane

Geometry	A_{1g}	E_g	T_{2g}
(x, x)	a^2	b^2	d^2
(x, y)	0	b^2	$\frac{2}{3}d^2$
(R, R)	0	$2b^2$	$\frac{4}{3}d^2$
(R, L)	a^2	0	$\frac{1}{3}d^2$

The second Raman scattering apparatus allowed us to obtain polarized spectra in the temperature range 300-15 K for frequencies down to 3.5 meV (triple monochromator option) and at temperatures down to 7 K with the spectral range limited by 12 meV at low frequencies (single monochromator and edge filter option). Selected spectra are shown in Fig. 1b, c. These measurements were done using the Jobin-Yvon T64000 triple monochromator spectrometer equipped with a liquid nitrogen cooled CCD detector with spectral resolution of 2 cm^{-1}. 514.5 nm line of Ar^+-Kr^+ mixed gas laser was used as the excitation light. The intensity of the incident light was 3 mW at 4 K and 10 meV above 4 K for single monochromator, and 15 meV for triple monochromator measurements. The laser heating was estimated to be about 1 K per 1mW. The measurements were performed in pseudo-Brewster's geometry using an elliptically shaped laser probe of 50 by 100 microns in size. The polarization-resolved spectra were measured in four configurations: $\hat{z}(xx)z$, $\hat{z}(xy)z$, $\hat{z}(RR)z$, and $\hat{z}(RL)z$, where $R(L)$ denotes the right (left) circular polarization, which allow to detect scattering channels of symmetries summarized in Table 1. For low temperature measurements the sample was mounted on the cold-finger of Janis ST-500 cryostat, which can be cooled down to 4 K without laser heating. The presented Raman response $\chi''(\omega, T)$ was normalized on the Bose-Einstein factor $[n(\omega, T) + 1]$, where $n(\omega, T) = [\exp(\hbar\omega/k_{\mathrm{B}}T) - 1]^{-1}$ is the Bose occupation factor.

To correct for the small deviations of the intensity of Raman response in different measurements, which were less than 20% for the same excitation power, all the spectra were normalized to the intensity of the A_{1g} phonon at 63 meV and the band at 82 meV.

Fitting of the experimental spectra was done by means of least squares assuming Lorentzian peak shapes for magnetic excitations and phonons, with the resulting function

$$\chi''(\omega) = \chi_0''(\omega) + \frac{1}{2\pi}\sum_{i=1}^{N}\frac{A_i\Gamma_i}{(\omega-\omega_i)^2 + (\Gamma_i/2)^2}, \tag{4}$$

where ω_i, Γ_i, and A_i correspond to the center, full width, and amplitude of the ith Lorentzian peak, and $\chi_0''(\omega)$ is the continuous electronic background. The detailed fitting results are shown in the supplement information.

Data availability

Data is available from the corresponding author on a reasonable request.

Received: 17 May 2025; Accepted: 17 July 2025;
Published online: 13 August 2025

References

1. Nagaosa, N. & Tokura, Y. Topological properties and dynamics of magnetic skyrmions. *Nat. Nanotechnol.* **8**, 899–911 (2013).
2. Fert, A., Cros, V. & Sampaio, J. Skyrmions on the track. *Nat. Nanotechnol.* **8**, 152–156 (2013).
3. Witczak-Krempa, W., Chen, G., Kim, Y. B. & Balents, L. Correlated quantum phenomena in the strong spin-orbit regime. *Annu. Rev. Condens. Matter Phys.* **5**, 57–82 (2014).

4. Takagi, H., Takayama, T., Jackeli, G., Khaliullin, G. & Nagler, S. E. Concept and realization of Kitaev quantum spin liquids. *Nat. Rev. Phys.* **1**, 264–280 (2019).
5. Broholm, C. et al. Quantum spin liquids. *Science* **367** (2020).
6. Nakatsuji, S. & Arita, R. Topological magnets: functions based on Berry phase and multipoles. *Annu. Rev. Condens. Matter Phys.* **13**, 119–142 (2022).
7. Armitage, N. P., Mele, E. J. & Vishwanath, A. Weyl and Dirac semimetals in three-dimensional solids. *Rev. Mod. Phys.* **90**, 015001–1– 015001–57 (2018).
8. Nakatsuji, S., Kiyohara, N. & Higo, T. Large anomalous Hall effect in a non-collinear antiferromagnet at room temperature. *Nature* **527**, 212 (2015).
9. Sakai, A. et al. Giant anomalous Nernst effect and quantum-critical scaling in a ferromagnetic semimetal. *Nat. Phys.* **14**, 1119–1124 (2018).
10. Liu, E. et al. Giant anomalous Hall effect in a ferromagnetic kagome-lattice semimetal. *Nat. Phys.* **14**, 1125–1131 (2018).
11. Liu, D. F. et al. Magnetic Weyl semimetal phase in a kagomé crystal. *Science* **365**, 1282–1285 (2019).
12. Belopolski, I. et al. Discovery of topological Weyl fermion lines and drumhead surface states in a room temperature magnet. *Science* **365**, 1278 (2019).
13. Nakatsuji, S. et al. Metallic spin-liquid behavior of the geometrically frustrated Kondo lattice $Pr_2Ir_2O_7$. *Phys. Rev. Lett.* **96**, 087204 (2006).
14. Machida, Y., Nakatsuji, S., Onoda, S., Tayama, T. & Sakakibara, T. Time-reversal symmetry breaking and spontaneous Hall effect without magnetic dipole order. *Nature* **463**, 210–213 (2010).
15. Pesin, D. & Balents, L. Mott physics and band topology in materials with strong spin–orbit interaction. *Nat. Phys.* **6**, 376–381 (2010).
16. Cheng, B. et al. Dielectric anomalies and interactions in the three-dimensional quadratic band touching Luttinger semimetal $Pr_2Ir_2O_7$. *Nat. Commun.* **8**, 1–6 (2017).
17. Ohtsuki, T. et al. Strain-induced spontaneous Hall effect in an epitaxial thin film of a Luttinger semimetal. *Proc. Natl. Acad. Sci.* **116**, 8803–8808 (2019).
18. Wan, X., Turner, A. M., Vishwanath, A. & Savrasov, S. Y. Topological semimetal and fermi-arc surface states in the electronic structure of pyrochlore iridates. *Phys. Rev. B* **83**, 205101 (2011).
19. Witczak-Krempa, W. & Kim, Y. B. Topological and magnetic phases of interacting electrons in the pyrochlore iridates. *Phys. Rev. B* **85**, 045124 (2012).
20. Bzdušek, T. C. V., Rüegg, A. & Sigrist, M. Weyl semimetal from spontaneous inversion symmetry breaking in pyrochlore oxides. *Phys. Rev*. **91**, 165105 (2015).
21. Matsuhira, K., Wakeshima, M., Hinatsu, Y. & Takagi, S. Metal–insulator transitions in pyrochlore oxides $Ln_2Ir_2O_7$. *J. Phys. Soc. Jpn.* **80**, 094701 (2011).
22. Nakayama, M. et al. Slater to Mott crossover in the metal to insulator transition of $Nd_2Ir_2O_7$. *Phys. Rev. Lett.* **117**, 056403 (2016).
23. Wang, K. et al. Unconventional free charge in the correlated semimetal $Nd_2Ir_2O_7$. *Nat. Phys.* **16**, 1194–1198 (2020).
24. Tomiyasu, K. et al. Emergence of magnetic long-range order in frustrated pyrochlore $Nd_2Ir_2O_7$ with metal–insulator transition. *J. Phys. Soc. Jpn.* **81**, 034709 (2012).
25. Guo, H. et al. Magnetic order in the pyrochlore iridate $Nd_2Ir_2O_7$ probed by muon spin relaxation. *Phys. Rev. B* **88**, 060411 (2013).
26. Asih, R. et al. Magnetic moments and ordered states in pyrochlore iridates $Nd_2Ir_2O_7$ and $Sm_2Ir_2O_7$ studied by muon-spin relaxation. *J. Phys. Soc. Jpn.* **86**, 024705 (2017).
27. Ueda, K. et al. Variation of charge dynamics in the course of metal-insulator transition for pyrochlore-type $Nd_2Ir_2O_7$. *Phys. Rev. Lett.* **109**, 136402 (2012).
28. Kondo, T. et al. Quadratic fermi node in a 3d strongly correlated semimetal. *Nat. Commun.* **6**, 10042 (2015).
29. Ueda, K. et al. Spontaneous Hall effect in the Weyl semimetal candidate of all-in all-out pyrochlore iridate. *Nat. Commun.* **9**, 1–7 (2018).
30. Nikolic, P., Xu, Y., Ohtsuki, T., Nakatsuji, S. & Drichko, N. Weyl-luttinger phase transition in pyrochlore iridates revealed by Raman scattering. *Phys. Rev. B* **110**, 035148 (2024).
31. Guo, H., Ritter, C. & Komarek, A. C. Direct determination of the spin structure of $Nd_2Ir_2O_7$ by means of neutron diffraction. *Phys. Rev. B* **94**, 161102 (2016).
32. Xu, J. et al. Magnetic structure and crystal-field states of the pyrochlore antiferromagnet $Nd_2Zr_2O_7$. *Phys. Rev. B* **92**, 224430 (2015).
33. Mauws, C. et al. Magnetic ordering in the ising antiferromagnetic pyrochlore Nd_2ScNbO_7. *J. Phys. Condens. Matter* **33**, 245802 (2021).
34. Ku, S. T. et al. Low temperature magnetic properties of $Nd_2Ru_2O_7$. *J. Phys. Condens. Matter* **30**, 155601 (2018).
35. Wulferding, D. et al. Collective magnetic Higgs excitation in a pyrochlore ruthenate. *npj Quantum Mater.* **8**, 40 (2023).
36. Tian, Z. et al. Field-induced quantum metal–insulator transition in the pyrochlore iridate nd2ir2o7. *Nat. Phys.* **12**, 134 (2016).
37. Chen, G. & Hermele, M. Magnetic orders and topological phases from *f-d* exchange in pyrochlore iridates. *Phys. Rev. B* **86**, 235129 (2012).
38. Lefrançois, E. et al. Anisotropy-tuned magnetic order in pyrochlore iridates. *Phys. Rev. Lett.* **114**, 247202 (2015).
39. Lefrançois, E. et al. Fragmentation in spin ice from magnetic charge injection. *Nat. Commun.* **8**, 209 (2017).
40. Guo, H., Ritter, C. & Komarek, A. C. Magnetic structure of $Tb_2Ir_2O_7$ determined by powder neutron diffraction. *Phys. Rev. B* **96**, 144415 (2017).
41. Cathelin, V. et al. Fragmented monopole crystal, dimer entropy, and coulomb interactions in $Dy_2Ir_2O_7$. *Phys. Rev. Res.* **2**, 032073 (2020).
42. Ross, K. A., Savary, L., Gaulin, B. D. & Balents, L. Quantum excitations in quantum spin ice. *Phys. Rev. X* **1**, 021002 (2011).
43. Savary, L. & Balents, L. Coulombic quantum liquids in spin-1/2 pyrochlores. *Phys. Rev. Lett.* **108**, 037202 (2012).
44. Gingras, M. J. & McClarty, P. A. Quantum spin ice: a search for gapless quantum spin liquids in pyrochlore magnets. *Rep. Prog. Phys.* **77**, 056501 (2014).
45. Hao, Z., Day, A. G. R. & Gingras, M. J. P. Bosonic many-body theory of quantum spin ice. *Phys. Rev. B* **90**, 214430 (2014).
46. Fu, J., Rau, J. G., Gingras, M. J. P. & Perkins, N. B. Fingerprints of quantum spin ice in raman scattering. *Phys. Rev. B* **96**, 035136 (2017).
47. Hasegawa, T. et al. Raman scattering study in iridium pyrochlore oxides. *J. Phys. Confer. Series* **200**, 012054 (2010).
48. Ueda, K. et al. Phonon anomalies in pyrochlore iridates studied by raman spectroscopy. *Phys. Rev. B* **100**, 115157 (2019).
49. Nguyen, T. H. et al. Topological magnon band crossing in $Y_2Ir_2O_7$. *Phys. Rev. Lett.* **127**, 267203 (2021).
50. Xu, Y. et al. Phonon spectrum of $Pr_2Zr_2O_7$ and $Pr_2Ir_2O_7$ as evidence of coupling of the lattice with electronic and magnetic degrees of freedom. *Phys. Rev. B* **105**, 075137 (2022).
51. Watahiki, M. et al. Crystalline electric field study in the pyrochlore $Nd_2Ir_2O_7$ with metal-insulator transition. In *Journal of Physics: Conference Series*, vol. 320, 012080 (IOP Publishing, 2011).
52. Xu, Y. et al. Importance of dynamic lattice effects for crystal field excitations in the quantum spin ice candidate $pr_2zr_2o_7$. *Phys. Rev. B* **104**, 075125 (2021).
53. Disseler, S. M. et al. Magnetic order and the electronic ground state in the pyrochlore iridate $Nd_2Ir_2O_7$. *Phys. Rev. B* **85**, 174441 (2012).
54. Sagayama, H. et al. Determination of long-range all-in-all-out ordering of Ir^{4+} moments in a pyrochlore iridate $Eu_2Ir_2O_7$ by resonant x-ray diffraction. *Phys. Rev. B* **87**, 100403 (2013).
55. Disseler, S. M. Direct evidence for the all-in/all-out magnetic structure in the pyrochlore iridates from muon spin relaxation. *Phys. Rev. B* **89**, 140413 (2014).

56. Sizyuk, Y., Price, C., Wölfle, P. & Perkins, N. B. Importance of anisotropic exchange interactions in honeycomb iridates: minimal model for zigzag antiferromagnetic order in Na_2IrO_3. *Phys. Rev. B* **90**, 155126 (2014).
57. Perkins, N. B., Sizyuk, Y. & Wölfle, P. Interplay of many-body and single-particle interactions in iridates and rhodates. *Phys. Rev. B* **89**, 035143 (2014).
58. Yang, Y., Li, M., Rousochatzakis, I. & Perkins, N. B. Non-loudon-fleury raman scattering in spin-orbit coupled mott insulators. *Phys. Rev. B* **104**, 144412 (2021).
59. Hwang, K., Trivedi, N. & Randeria, M. Topological magnons with nodal-line and triple-point degeneracies: Implications for thermal hall effect in pyrochlore iridates. *Phys. Rev. Lett.* **125**, 047203 (2020).
60. Fleury, P. & Loudon, R. Scattering of light by one-and two-magnon excitations. *Phys. Rev.* **166**, 514 (1968).
61. Rosalin, M., Telang, P., Singh, S., Muthu, D. & Sood, A. Magnon excitation and spin-phonon coupling in $A_2Ir_2O_7$ (A = Gd, Dy, and Er). *Phys. Rev. B* **109**, 184434 (2024).
62. Muhammad, S. et al. Probing scattering of Raman phonons on magnetic and electronic excitations in pyrochlores $Nd_2Zr_2O_7$ and $Nd_2Ir_2O_7$. *arXiv preprint arXiv:2501.13326* (2025).
63. Petit, S. et al. Observation of magnetic fragmentation in spin ice. *Nat. Phys.* **12**, 746–750 (2016).
64. Benton, O. Quantum origins of moment fragmentation in $Nd_2Zr_2O_7$. *Phys. Rev. B* **94**, 104430 (2016).
65. Léger, M. et al. Spin dynamics and unconventional coulomb phase in $Nd_2Zr_2O_7$. *Phys. Rev. Lett.* **126**, 247201 (2021).
66. Anand, V. K. et al. Observation of long-range magnetic ordering in pyrohafnate $Nd_2Hf_2O_7$: a neutron diffraction study. *Phys. Rev. B* **92**, 184418 (2015).
67. Kapon, I. et al. Magnetic field tuning of valley population in the weyl phase of $Nd_2Ir_2O_7$. *Phys. Rev. Res.* **4**, 023056 (2022).
68. Richard, P., Poirier, M. & Jandl, S. Low-temperature magnetism of Nd_2CuO_4: an ultrasonic investigation. *Phys. Rev. B* **71**, 144425 (2005).
69. Gaudet, J. et al. Weyl-mediated helical magnetism in ndalsi. *Nat. Mater.* **20**, 1650–1656 (2021).
70. Lygouras, C. J. et al. Magnetic excitations and interactions in the Weyl ferrimagnet NdAlSi. *arXiv preprint arXiv:2412.20743* (2024).
71. Drucker, N. C. et al. Topology stabilized fluctuations in a magnetic nodal semimetal. *Nat. Commun.* **14**, 5182 (2023).
72. Cottam, M. G. & Lockwood, D. J. *Light scattering in magnetic solids* (Wiley New York, 1986).
73. Nguyen, T. M. H. et al. Two-magnon scattering in the 5 d all-in-all-out pyrochlore magnet $Cd_2Os_2O_7$. *Nat. Commun.* **8**, 1–8 (2017).
74. Xu, J. et al. Order out of a coulomb phase and higgs transition: frustrated transverse interactions of nd 2 zr 2 o 7. *Phys. Rev. Lett.* **124**, 097203 (2020).
75. Bouaziz, J., Bihlmayer, G., Patrick, C. E., Staunton, J. B. & Blügel, S. Origin of incommensurate magnetic order in the R alsi magnetic weyl semimetals (R = Pr, Nd, Sm). *Phys. Rev. B* **109**, L201108 (2024).
76. Millican, J. N. et al. Crystal growth and structure of $R_2Ir_2O_7$ (R = pr, eu) using molten kf. *Mater. Res. Bull.* **42**, 928–934 (2007).

Acknowledgements

The authors are thankful to C. Broholm and S. Wilson for useful discussions. This work was supported as part of the Institute for Quantum Matter, an Energy Frontier Research Center funded by the U.S. Department of Energy, Office of Science, Basic Energy Sciences under Award No. DE- SC0019331. Additional support came for work at JHU from the gift of William H. Miller III. Work in Japan is partially supported by CREST (Grant Number: JPMJCR18T3 and JPMJCR15Q5), by New Energy and Industrial Technology Development Organization (NEDO), by Grants-in-Aids for Scientific Research on Innovative Areas (Grant Number: 15H05882 and 15H05883) from the Ministry of Education, Culture, Sports, Science, and Technology of Japan, and by Grants-in-Aid for Scientific Research (Grant Number: 19H00650). The work of Y.Y. and N.B.P. was supported by the U.S. Department of Energy, Office of Science, Basic Energy Sciences under Award No. DE-SC0018056. N.B.P. also acknowledges the hospitality and partial support of the Technical University of Munich – Institute for Advanced Study and the Alexander von Humboldt Foundation..

Author contributions

N.D. conceived the idea of the experiment. T.O., and Y.Q., and S.N. grew the crystals. Y.X., J.T., and N.D. collected and analyzed the Raman scattering data. Y.Y. and N.P. calculated the magnon dispersion and two-spinon excitations. N.D., D.v.d.M., Y.Y., Y.X., and N.P. wrote the manuscript.

Competing interests

The authors declare no competing interests.

Additional information

Supplementary information The online version contains supplementary material available at https://doi.org/10.1038/s41535-025-00806-y.

Correspondence and requests for materials should be addressed to Natalia Drichko.